




Di-Higgs production in SUSY models at the LHC

Peisi Huang^a, Yu Hang Ng^b 

Department of Physics and Astronomy, University of Nebraska-Lincoln, Lincoln, NE 68588, USA

Received: 9 April 2020 / Accepted: 7 August 2020 / Published online: 17 August 2020
© Società Italiana di Fisica and Springer-Verlag GmbH Germany, part of Springer Nature 2020

Abstract We study the modification to di-Higgs production via gluon fusion within the context of the minimal supersymmetric standard model and the next-to-minimal supersymmetric standard model in the parameter space allowed by current experimental and theoretical constraints, and also relevant to the Large Hadron Collider (LHC) experiments in the near future. The calculation is based on the analytical expression of the leading-order Feynman amplitudes (which includes both quark and squark loops). We separate the di-Higgs production cross section into resonant, non-resonant, and interference parts, in order to better understand the mechanisms that are responsible for the modification to di-Higgs production rate in different regions of the allowed parameter space. We also investigate the sensitivity of high-luminosity LHC (HL-LHC) to the di-Higgs production in these low-energy supersymmetry models. Furthermore, we examine the complementarity between di-Higgs searches and direct searches for BSM particles and precision Higgs couplings measurements at the HL-LHC. We found that the di-Higgs production cross section can be enhanced significantly through resonant production. In the region where the resonant production cross section is small, di-Higgs production receives a moderate enhancement due to the modifications in the Higgs couplings. In addition, there is a strong correlation between di-Higgs production and single Higgs production, and di-Higgs production is not as sensitive as single Higgs production at the HL-LHC.

1 Introduction

The Higgs boson discovery by the CMS and ATLAS experiments in 2012 [1, 2] is the first and a crucial step in understanding the mechanism of the electroweak symmetry breaking. The Higgs properties, including the mass, spin, parity, and its couplings to other standard model (SM) particles have been measured with high precision in the subsequent analyses [3–6]. However, we know very little about the Higgs potential. In the SM, the Higgs potential is

$$V = -\mu^2 \phi^\dagger \phi + \lambda (\phi^\dagger \phi)^2, \quad (1)$$

which is completely specified by two parameters μ and λ . μ and λ can be determined from the vacuum expectation value (vev) of the Higgs field, and the mass of the Higgs boson, but there is no direct measurement beyond that. Thus, the next step in understanding the shape of

^a e-mail: peisi.huang@unl.edu

^b e-mail: yu-hang.ng@huskers.unl.edu (corresponding author)

the Higgs potential is to measure the Higgs trilinear coupling. The Higgs trilinear coupling can be probed by the di-Higgs production at the LHC.

Di-Higgs production is sensitive to new physics, including new scalar resonances [7–14], new colored particles [10–13, 15–17], and modified Higgs couplings [8, 10–14, 17, 18], and therefore can be complementary to direct searches of new particles, and precision Higgs coupling measurements. In particular, in this paper, we consider di-Higgs production with low-energy supersymmetry (SUSY) models.

In low-energy SUSY models, the di-Higgs production rate can be modified through various mechanisms. First, the Higgs sector is extended by introducing an additional Higgs doublet, in the minimal supersymmetric extension of the SM (MSSM) and an additional singlet in the next-to-minimal supersymmetric extension of the SM (NMSSM). The additional neutral Higgs states can be produced at the LHC and can decay into a pair of SM-like Higgs bosons, and therefore contribute to di-Higgs production. Second, the low-energy SUSY models allow the presence of new light colored particles coupled strongly to the Higgs. Those new colored particles give new QCD loop diagrams contributing to di-Higgs production [15–17]. There will be new interference terms arising from those new diagrams as well [19, 20]. Third, in SUSY models, Higgs couplings, including Higgs couplings to SM particles, and the Higgs self-couplings, may present small deviations with respect to the SM ones, resulting in modified di-Higgs production [17]. The modified couplings also change the decay of the Higgs, resulting in additional modifications in specific channels. In this paper, we study the di-Higgs production in the MSSM and the NMSSM, with a focus on identifying the dominant contribution in different regions of parameter space. We also study the complementarity between di-Higgs searches and other searches, such as direct searches for new scalars, and precision Higgs measurements at the HL-LHC.

This article is structured as follows. In Sect. 2, we calculate the leading-order di-Higgs production cross section in the MSSM and the NMSSM. In Sect. 3, we present the main results of this paper. First, we identify the parameter space that satisfies current experimental constraints and theoretical requirements. Then, we show the results of di-Higgs production cross section in the $b\bar{b}\tau^+\tau^-$ and $b\bar{b}\gamma\gamma$ final states, in those regions. Furthermore, we study the complementarity of di-Higgs with other searches. We also discuss the resonant, non-resonant, and interference contributions of the di-Higgs production in different regions of the parameter space. Finally, we reserve Sect. 4 for a summary of the main results.

2 Matrix elements and cross sections

The dominant di-Higgs production mode at the LHC is the gluon–gluon fusion (ggF) process. The rate of di-Higgs production from bottom-quark fusion can potentially be significant [12, 21, 22], but it is subdominant in our models parameter spaces that are allowed by the current experimental constraints (see Fig. 2 and Table 1). In the SM, there are two diagrams contributing to the di-Higgs production via gluon fusion at the leading order (LO), the triangle diagram (diagram (1) in Fig. 1, with $H_i = h$), and the box diagram (diagram (2) in Fig. 1). In this section, we calculate the leading-order di-Higgs production cross section $\sigma(pp \rightarrow gg \rightarrow hh)$ at $\sqrt{s} = 14$ TeV by using the analytical expressions for one-loop amplitudes of $gg \rightarrow hh$ in the MSSM and the NMSSM.

In the SM, the analytical expression for LO di-Higgs production via ggF was studied in [23]. In the MSSM, the quark and squark loop contributions to LO pair production of neutral Higgs bosons via ggF were first given by [24, 25], respectively. There is also a publicly available Fortran program **HPAIR** that calculates the quark loop contributions to the cross

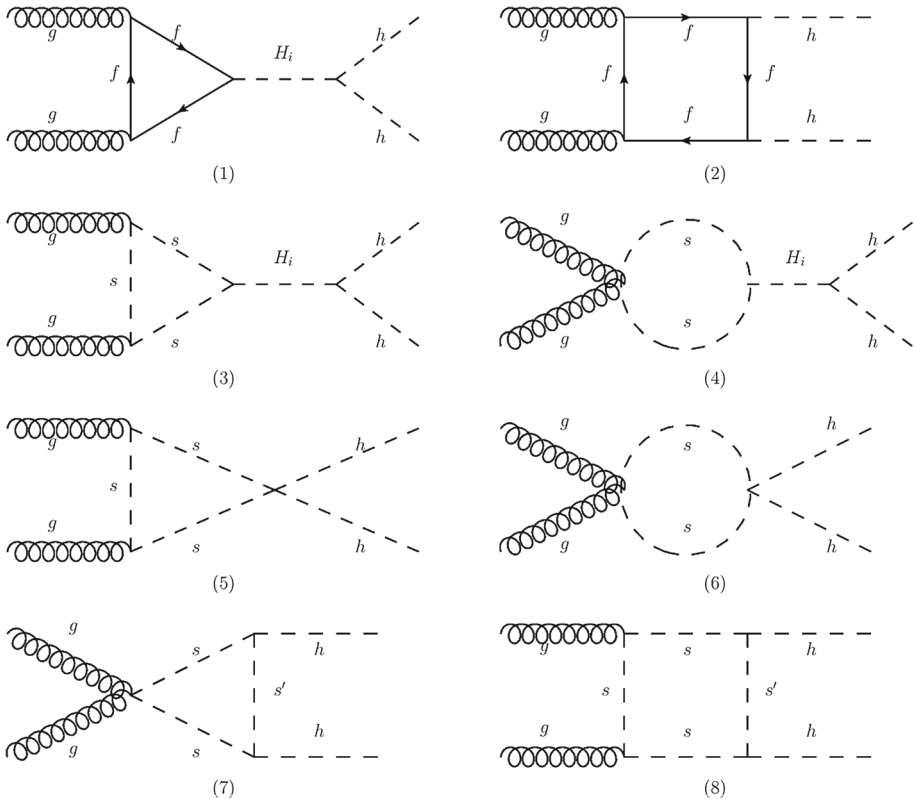


Fig. 1 Leading-order Feynman diagrams for di-Higgs production in the MSSM at LHC. H_i are CP-even Higgs bosons, f are top and bottom quarks, and s, s' are stops

section of neutral Higgs bosons pair production via ggF in both SM and MSSM cases, and includes NLO QCD correction in the heavy top quark limit [26]. There is no publicly available code calculating the di-Higgs production cross section in the NMSSM. In this work, we write our own Mathematica programs to calculate the MSSM and the NMSSM di-Higgs production cross section to get more control over the calculations and results. The MSSM and NMSSM couplings, masses, and decay widths of Higgs bosons are calculated by using **FeynHiggs-2.14.3** [27–33] and **NMSSMTools-5.4.1** [34–39], respectively. The quark loop parts of our MSSM results agree with **HPAIR**, which does not include squark loops. (The particle spectrum and couplings calculated by **HPAIR** differ from those calculated by **FeynHiggs-2.14.3**. To compare the di-Higgs cross section calculation, we modified the **HPAIR** program such that it took the particle spectrum and the couplings from **FeynHiggs-2.14.3**.)

2.1 MSSM

In the MSSM, since the superpotential is holomorphic, two distinct Higgs doublets are introduced in order to give masses to up-type and down-type fermions, respectively. Furthermore, the introduction of two Higgs doublets with opposite hypercharges also leads to the successful cancellation of chiral anomalies due to the Higgsinos [40,41]. The two Higgs doublets give rise to two neutral CP-even Higgs bosons, one neutral CP-odd Higgs boson, and a pair of

charged Higgs bosons. In this work, we assume that the lighter CP-even neutral Higgs boson to be SM-like, and denote the SM-like Higgs boson as h , and the heavy CP-even neutral heavy Higgs boson as H . The heavy Higgs can be produced through quark and squark loops and can decay to a pair of SM Higgs bosons, as shown in diagrams (1), (3), and (4) in Fig. 1 with $H_i = H$. The squarks also lead to new diagrams that contribute to di-Higgs production, as shown in diagrams (3)–(8) in Fig. 1. The corresponding spin and color averaged partonic differential cross section is

$$\frac{d\hat{\sigma}}{d\hat{t}} = \frac{(\alpha_s(Q))^2}{2^{13}\pi^3} (|A|^2 + |B|^2), \tag{2}$$

where the matrix elements are separated by the helicities of the initial gluons. $A_{(i)}$ are matrix elements of the i -th diagram in Fig. 1 when helicities of initial gluons are identical, and $B_{(i)}$ are matrix elements of the i -th diagram in Fig. 1 when helicities of initial gluons are opposite. A and B denote the sum of those matrix elements.

$$\begin{aligned} A &= \sum_{H_i=h,H} \sum_{f=b,t} A_{(1)}(f, H_i) + \sum_{f=b,t} A_{(2)}(f) + \sum_{H_i=h,H} \sum_{s=\tilde{t}_1, \tilde{t}_2} A_{(3+4)}(s, H_i) \\ &+ \sum_{s=\tilde{t}_1, \tilde{t}_2} A_{(5+6)}(s) + \sum_{s'=\tilde{t}_1, \tilde{t}_2} \sum_{s=\tilde{t}_1, \tilde{t}_2} A_{(7+8)}(s, s'), \\ B &= \sum_{f=b,t} B_{(2)}(f) + \sum_{s'=\tilde{t}_1, \tilde{t}_2} \sum_{s=\tilde{t}_1, \tilde{t}_2} B_{(8)}(s, s'). \end{aligned}$$

The matrix elements $A_{(i)}$ and $B_{(i)}$ read,

$$A_{(1)}(f, H_i) = \frac{g_{H_i h h} g_{H_i f f}}{m_f} \frac{F_{\triangleright}^{(1/2)}(m_f)}{\hat{s} - m_{H_i}^2 + i\Gamma_{H_i} m_{H_i}} \tag{3}$$

$$A_{(2)}(f) = \left(\frac{g_{h f f}}{m_f}\right)^2 F_{\square}^{(1/2)}(m_f) \tag{4}$$

$$B_{(2)}(f) = \left(\frac{g_{h f f}}{m_f}\right)^2 G_{\square}^{(1/2)}(m_f) \tag{5}$$

$$A_{(3+4)}(s, H_i) = \frac{g_{H_i h h} g_{H_i s s}}{2m_s^2} \frac{F_{\triangleright}^{(0)}(m_s)}{\hat{s} - m_{H_i}^2 + i\Gamma_{H_i} m_{H_i}} \tag{6}$$

$$A_{(5+6)}(s) = -\frac{g_{h s s}}{2m_s^2} F_{\triangleright}^{(0)}(m_s) \tag{7}$$

$$A_{(7+8)}(s, s') = \frac{g_{h s s'}^2}{2m_s^2 m_{s'}^2} F_{\square}^{(0)}(m_s, m_{s'}) \tag{8}$$

$$B_{(8)}(s, s') = \frac{g_{h s s'}^2}{2m_s^2 m_{s'}^2} G_{\square}^{(0)}(m_s, m_{s'}). \tag{9}$$

Expressions for the form factors (F_{\triangleright} , F_{\square} , G_{\square}) are given in Appendix A. \hat{s} , \hat{t} , \hat{u} are Mandelstam variables. In our calculations, we include the dominant fermion contributions from top and bottom loops, and sfermion contributions from stops and sbottoms. We choose $Q = m_{hh}/2$, where m_{hh} is the invariant mass of the SM-like Higgs pair.

We separate the differential cross sections into resonant, non-resonant, and interference contributions as

$$\frac{d\hat{\sigma}_{\text{res}}}{d\hat{t}} = \frac{(\alpha_s(Q))^2}{2^{13}\pi^3} |A_{\text{res}}|^2, \tag{10}$$

$$\frac{d\hat{\sigma}_{\text{nr}}}{d\hat{t}} = \frac{(\alpha_s(Q))^2}{2^{13}\pi^3} (|A_{\text{nr}}|^2 + |B_{\text{nr}}|^2), \tag{11}$$

$$\frac{d\hat{\sigma}_{\text{int}}}{d\hat{t}} = \frac{(\alpha_s(Q))^2}{2^{13}\pi^3} (2 \text{Re}(A_{\text{res}} \cdot A_{\text{nr}}^*)), \tag{12}$$

where

$$A_{\text{res}} = \sum_{f=b,t} A_{(1)}(f, H) + \sum_{s=\tilde{t}_1, \tilde{t}_2} A_{(3+4)}(s, H),$$

$$A_{\text{nr}} = A - A_{\text{res}},$$

$$B_{\text{nr}} = B.$$

The resonant amplitude is defined such that it has a pole in the region of interest (see Fig. 2). The non-resonant amplitude includes all other Feynman diagrams, and the interference cross section corresponds to the interference between resonant and non-resonant amplitude, as the name suggests.

The total cross section corresponding to each partonic cross section can be obtained by using

$$\sigma(pp \rightarrow gg \rightarrow hh) = \int_{(2m_h)^2}^{(14\text{TeV})^2} d\hat{s} \frac{d\mathcal{L}_{gg}}{d\hat{s}} \hat{\sigma}, \tag{13}$$

where $\frac{d\mathcal{L}_{gg}}{d\hat{s}}$ is the differential gluon–gluon luminosity as defined in [42]. We have adopted MSTW2008 parton distributions for the cross sections calculation [43], and used **ManeParse** to process the parton distribution functions [44].

The NLO QCD corrections (when the loop particles are heavy) can increase the leading-order SM and MSSM di-Higgs production cross sections by about a factor of two [45]. Currently, the full NLO QCD corrections are known in the SM case [46–48], but not yet available in the MSSM case [49]. Thus, we normalize our leading-order cross sections with respect to the SM leading-order cross section.

2.2 NMSSM

The MSSM superpotential contains a dimensionful parameter μ , which is naively expected to be $\sim M_{\text{GUT}}$ or $\sim M_{\text{Planck}}$, but phenomenology demands it to be of order of SUSY breaking scale in order to avoid too much fine-tuning [50–52]. This is known as the μ problem. One of the solutions is the NMSSM, which is a singlet extension of MSSM. In the NMSSM, an effective μ -term is generated dynamically (see Eq. (15)). In addition, the upper bound on the tree-level mass of the lightest neutral CP-even Higgs receives an additional positive contribution $\lambda^2 v^2 \sin^2(2\beta)$ [53]. Thus, when $\tan \beta$ is not too large, $m_h \approx 125\text{GeV}$ may be achieved without the need for large radiative corrections, resulting less fine-tuning than in the MSSM.

The NMSSM has one extra supermultiplet as compared to the MSSM, i.e., the gauge singlet chiral superfield \hat{S} , which contains one complex spin-0 singlet (S) and one spin-1/2 singlino (\tilde{S}). S gives rise to one neutral CP-even Higgs and one neutral CP-odd Higgs.

In this article, we only consider the \mathbb{Z}_3 -invariant NMSSM, which has the scale invariant superpotential W_{Higgs} given by

$$W_{\text{Higgs}} = \lambda \hat{S} \hat{H}_u \cdot \hat{H}_d + \frac{\kappa}{3} \hat{S}^3, \tag{14}$$

where W_{Higgs} is the part of superpotential that depends exclusively on Higgs superfields \hat{H}_u , \hat{H}_d , and \hat{S} . In the next paragraph, we will briefly introduce the notations and sign conventions of relevant NMSSM parameters that appear in this paper. Please refer to the review paper [53] for more details about the NMSSM.

The first term in Eq. (14) replaces the $\mu \hat{H}_u \cdot \hat{H}_d$ term in MSSM superpotential, and generates the effective μ -term at electroweak scale when S acquires a non-vanishing vev:

$$\mu_{\text{eff}} = \lambda \langle S \rangle. \tag{15}$$

v_u and v_d are vevs of H_u^0 and H_d^0 , respectively, and

$$\tan \beta = \frac{v_u}{v_d}. \tag{16}$$

A_λ and A_κ are trilinear soft SUSY breaking couplings corresponding to the first and second term in Eq. (14), respectively. M_1 , M_2 , and M_3 are soft SUSY breaking masses of $U(1)_Y$ gaugino, $SU(2)$ gauginos, and $SU(3)$ gauginos, respectively. We choose $\tan \beta$ and λ to be positive, while μ_{eff} , κ , A_λ , A_κ can have both signs.

The set of leading-order Feynman diagrams for $gg \rightarrow hh$ in NMSSM is the same as the MSSM case, except that there are three neutral CP-even Higgs bosons ($H_i = H_1, H_2, H_3$, ordered by ascending mass) in NMSSM. Thus, Eqs. (3–9) are still valid in the NMSSM case.

3 Phenomenological study

3.1 MSSM

In the MSSM study, for the stops to contribute in a relevant way, the stop should not be too far away from the weak scale [17]. Therefore, we chose the lighter stop mass to be 600 GeV, which is right above the current LHC limit [54,55]. To allow for large mixings in the stop sector, which can enhance the di-Higgs production rate through diagrams (7) and (8) in Fig. 1, we choose the heavier stop mass to be 5 TeV. The stop mixing parameter X_t is chosen so that the SM-like Higgs mass is 125 GeV. We calculated the SM-like Higgs mass using **FeynHiggs-2.14.3** [27–33], and found that in the region of interest, there always exists a value of X_t such that $m_h = 125$ GeV. Furthermore, X_t cannot be too large in order to have a stable SM-like vacuum. Here, we use the approximate bound [56]:

$$\left(X_t + \frac{\mu}{\tan \beta} \right)^2 \leq 3.4 \left(m_{\tilde{Q}_3}^2 + m_{\tilde{t}_R}^2 \right) + 0.5 |m_{\tilde{Q}_3}^2 - m_{\tilde{t}_R}^2| + 60 \left(\frac{m_Z^2}{2} \cos 2\beta + m_A^2 \cos^2 \beta \right). \tag{17}$$

We checked that this bound is satisfied by every point in the parameter space that is shown in Fig. 2.

Then, we fix the masses and the mixings in the sbottom sector by imposing $m_{\tilde{t}_R} = m_{\tilde{b}_R}$, and $A_t = A_b$. We ignore the contributions from all other sfermions and electroweakinos. When the electroweakinos are lighter than $m_H/2$, the heavy Higgs starts to decay to a pair

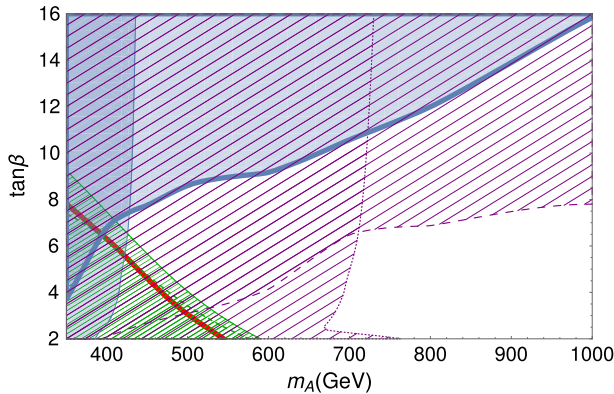


Fig. 2 The MSSM parameter space with current experimental constraints and projected sensitivities. The blue shaded region is excluded by current experiment constraints. The purple and green shaded region can be reached by HL-LHC. The red solid line represents the case when resonant cross section equals to non-resonant cross section

of electroweakinos, which reduces its branching ratio to a pair of SM Higgs, and therefore reduces the resonant di-Higgs production cross section. As we aim to understand how large the di-Higgs production cross section can be at the LHC, we ignore the contributions from electroweakinos.

Based on those considerations, we keep m_A , the mass of the CP-odd Higgs boson, and $\tan \beta$, the ratio between two vevs, as free parameters in our study. The ranges of m_A and $\tan \beta$ are restricted by several experimental observations and theoretical requirements as shown in Fig. 2. First, the Higgs couplings depend strongly on the mixing between the SM-like Higgs and the new CP-even Higgs, and in the region of interest, can deviate significantly from the SM. Therefore, the parameter space is restricted by precision Higgs measurements, and the most stringent limit comes from the Higgs boson coupling to bottom-quark measurement at ATLAS [6]. The blue shaded region with the thin solid boundary line is excluded by the precision measurement of Higgs couplings at $\sqrt{s} = 13$ TeV [6,57]. Second, the heavy neutral Higgs couples to the SM particles, and can be searched for through its decays. The most sensitive channel is in the di-tau final state, and the blue shaded region with the thick solid boundary line is excluded by the search for the additional neutral Higgs bosons in the di-tau final state at $\sqrt{s} = 13$ TeV [58,59]. In the parameter space of interest, the constraints from the direct searches for the charged Higgs are weaker than the two experimental constraints stated above [60–64]. A charged Higgs also contributes to the low-energy precision flavor observables (such as $B_s \rightarrow \mu^+ \mu^-$ and $B \rightarrow X_s \gamma$). As shown in [65,66], the charged Higgs contribution to the flavor observables are very well within the current experimental sensitivity in the region of interest (see Fig. 2).

We calculate the leading-order di-Higgs production cross section as described in the previous section, and the results are shown in Fig. 3. To account for the modifications in the Higgs decay, we show the results in the two most sensitive channels, $bb\gamma\gamma$ and $bb\tau\tau$, according to the ATLAS projections [67]. In the region of interest, $B(h \rightarrow b\bar{b})B(h \rightarrow \tau^+\tau^-)$ is always enhanced, and it can be enhanced up to 25% compared to the SM value, while $B(h \rightarrow b\bar{b})B(h \rightarrow \gamma\gamma)$ is suppressed in most of the parameter space, and it can be suppressed up to 14% compared to the SM value. The di-Higgs production rate can be enhanced significantly in the region where m_A and $\tan \beta$ are small. For instance, when

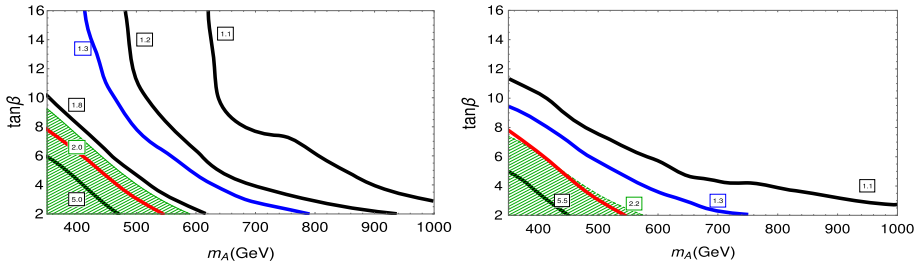


Fig. 3 Contour plots for $\sigma(pp \rightarrow hh \rightarrow b\bar{b}\tau^+\tau^-)$ (left panel) and $\sigma(pp \rightarrow hh \rightarrow b\bar{b}\gamma\gamma)$ (right panel) normalized to SM value at $\sqrt{s} = 14$ TeV. The numbers in the boxes are $\sigma(pp \rightarrow hh \rightarrow b\bar{b}\tau^+\tau^-)/\sigma_{SM}$ (left panel) and $\sigma(pp \rightarrow hh \rightarrow b\bar{b}\gamma\gamma)/\sigma_{SM}$ (right panel), respectively. The cross sections in the shaded regions are outside the 95% CL of the projected di-Higgs production cross section at HL-LHC

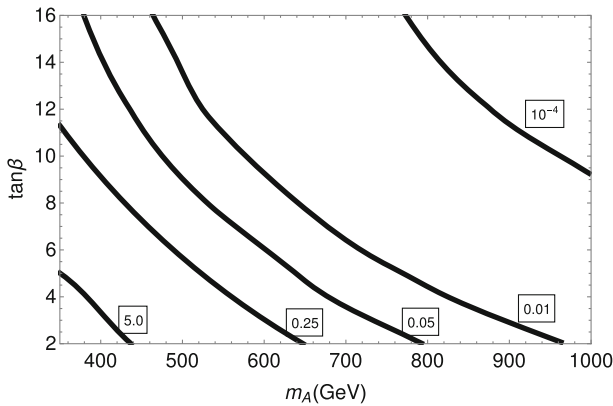


Fig. 4 Resonant contribution of di-Higgs production cross section (normalized to SM value) at $\sqrt{s} = 14$ TeV. The numbers in the boxes are σ_{res}/σ_{SM}

$m_A = 400$ GeV and $\tan \beta = 2$, $\sigma(pp \rightarrow hh \rightarrow b\bar{b}\tau^+\tau^-)/SM = 13.7$ and $\sigma(pp \rightarrow hh \rightarrow b\bar{b}\gamma\gamma)/SM = 11.3$. This enhancement is mainly due to the large resonant contribution of di-Higgs production in this region, which can also be seen in Fig. 4.

In Fig. 4, we plot the resonant production of di-Higgs normalized to the SM production rate. The production rate can be up to 5 times the SM value when m_A and $\tan \beta$ are small, and decreases quickly as m_A and $\tan \beta$ increase as expected.

Outside the region where di-Higgs production receives a large correction from the resonant production, the modifications come from the non-resonant production. The non-resonant di-Higgs production is very close to the SM contribution in the whole region of interest (see Fig. 2). Our calculations show that $\kappa_t = g_{htt}/g_{htt}^{SM}$ varies between 0.95 and 1, while $\lambda_3 = (g_{hhh} - g_{hhh}^{SM})/g_{hhh}^{SM}$ varies between -0.24 and -0.12 in the parameter space of interest (see Fig. 2). The decrease in the SM-like Higgs self-coupling reduces the destructive interference between the triangle diagram and the fermionic box diagram (i.e., first and second diagrams in Fig. 1); hence, it enhances non-resonant di-Higgs production cross section. However, this effect is offset by a small decrease in κ_t . The box diagram, which dominates over the triangle diagram, is proportional to κ_t^4 , so the di-Higgs rate is very sensitive to the value of κ_t . Therefore, a small decrease in κ_t offsets the decrease in λ_3 . As a result, the non-resonant di-Higgs cross section is only larger than the SM di-Higgs production cross section by a

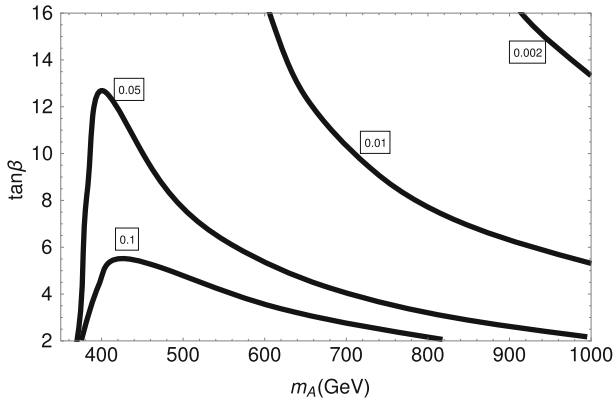


Fig. 5 Interference (normalized to SM value) between resonant and non-resonant amplitude at $\sqrt{s} = 14$ TeV

few percent in most of the parameter space (the effects of λ_3 and κ_t on di-Higgs production cross section was also discussed in [68,69]). The interference between the resonant and non-resonant amplitude is small over the whole parameter space, which we plot in Fig. 5.

Contribution from stop loops is less than 3% of the total di-Higgs production cross section. Therefore, in the MSSM case, the major modification to di-Higgs production is from the new resonance, which is the new CP-even neutral Higgs, and the modifications to the branching ratios.

It is known that the theoretical calculation of SM di-Higgs production cross section has large QCD scale uncertainty at the level of 15% to 20% [48]. In Fig. 3, we overlay the di-Higgs production cross section with a 30% uncertainty line (the blue line) to remind the reader that the modifications in the total di-Higgs production within 30%, (above the blue line) can be due to the QCD scale uncertainty and not be treated as a hint for new physics. We estimate the QCD scale uncertainty by varying the renormalization scale by a factor of two up and down around our central scale choice $Q = m_{hh}/2$ and found a similar QCD scale uncertainty.

We also study the complementarity between di-Higgs and other Higgs studies. In Fig. 2, we compare the projected sensitivity in the $bb\gamma\gamma$ and the $bb\tau\tau$ channels [67,70] with other searches. We separate the parameter space into two regions, the one below the red solid line is dominated by resonant production, while the region above the red solid line is dominated by non-resonant production. The green shaded region with solid boundary line and the dashed boundary line shows the region that can be excluded by the non-resonant $bb\tau\tau$ and $bb\gamma\gamma$ searches at HL-LHC with 3000 fb^{-1} , respectively, [67,70]. The projected sensitivity for the resonant production is not available at present, but we do expect that is better compared to the sensitivity for the non-resonant production. Therefore, the whole green shaded region can be probed by HL-LHC. The purple shaded region with the dotted boundary line shows the region that can be tested by the projected Higgs boson couplings measurements at HL-LHC [71]. The purple shaded region with the dashed boundary line shows the projected reach for the additional neutral Higgs bosons in the di-tau final state at HL-LHC at 95% C.L. [72]. From Fig. 2, a large fraction of the parameter space that is not excluded by current experimental constraints will be tested by the HL-LHC experiments (i.e., the purple and green region). The di-Higgs production is not as sensitive as other searches, but provides a complementary probe at the HL-LHC.

Table 1 NMSSM parameter space

| | $\tan\beta$ | λ | κ | A_λ | A_κ | μ_{eff} | M_1 | M_2 | M_3 | A_t | A_b | A_τ | $m_{\tilde{Q}_3}$ | $m_{\tilde{L}_3}$ |
|-----|-------------|-----------|----------|-------------|------------|--------------------|-------|-------|-------|-------|-------|----------|-------------------|-------------------|
| | (in TeV) | | | | | | | | | | | | | |
| min | 1 | 0 | -0.7 | -1 | -1 | -0.5 | 0.1 | 0.2 | 1.3 | -6 | -6 | -3 | 0.6 | 0.6 |
| max | 10 | 0.7 | 0.7 | 1 | 1 | 0.5 | 1 | 2 | 7 | 6 | 6 | 3 | 4 | 4 |

3.2 NMSSM

In the NMSSM study, we perform a random scan over the NMSSM parameter space using **NMSSMTools-5.4.1** as there are more relevant parameters. A similar study can be found in [73]. The range of the parameters is as shown in Table 1. We also assume

$$m_{\tilde{\tau}_R} = m_{\tilde{Q}_3}, \quad m_{\tilde{\tau}_L} = m_{\tilde{L}_3}, \quad m_{\tilde{b}_R} = 3 \text{ TeV}, \tag{18}$$

although we expect the sfermion contributions are negligible, as in the MSSM case. We require the mass of one of the NMSSM neutral CP-even Higgs bosons to be $125.26 \pm 3 \text{ GeV}$ to accommodate experimental and theoretical uncertainties up to 3 GeV. Besides that, λ and κ have to be sufficiently small so that perturbation theory remains valid. Here, we use [74]

$$\lambda^2 + \kappa^2 < 0.7^2. \tag{19}$$

Constraints from collider experiments (LEP, Tevatron, LHC) and dark matter direct detection experiments are also checked by using **NMSSMTools-5.4.1** [34–39, 75–77]. All points in Fig. 6 also satisfy the constraint on dark matter relic density from *Planck* measurement [78] (including +10% uncertainty in theoretical calculation)

$$\Omega_{\tilde{\chi}_1^0} h^2 \leq 0.131. \tag{20}$$

Our results for the NMSSM are shown in Fig. 6, for each point surviving all constraints, we plot the di-Higgs production cross section in the $bb\tau^+\tau^-$ channel (upper panel) and the $bb\gamma\gamma$ channel (lower panel). The $B(h \rightarrow \tau^+\tau^-)/\text{SM}$ and $B(h \rightarrow \gamma\gamma)/\text{SM}$ tend to be anticorrelated, and their modifications are of the same order. In the region of interest, $B(h \rightarrow b\bar{b})B(h \rightarrow \tau^+\tau^-)$ can be enhanced up to 16% compared to the SM value, and $B(h \rightarrow b\bar{b})B(h \rightarrow \gamma\gamma)$ can be suppressed up to 10% compared to the SM value. The NMSSM di-Higgs production cross sections can be enhanced significantly compared to the SM. Similar to the MSSM case, the interference between the resonant and non-resonant amplitude and the contributions from squark loops are small over the whole parameter space. When the new CP-even Higgs states are light, the dominant contribution is from resonant di-Higgs production. The resonant di-Higgs rate can be a few times the SM rate. The non-resonant contribution of di-Higgs production is generally enhanced by 20% to 60%, which comes from the decrease in the SM-like Higgs self-coupling. In the region of interest, δ_3 generally varies between -0.3 and -0.58 , resulting in the 20% to 60% enhancement in the non-resonant production. Here, we use the projected sensitivity of the non-resonant production, and we expect it to be better for resonant productions.

Unlike the MSSM case, κ_t is very close to unity in the NMSSM case, and therefore, the enhancement due to the suppression in λ_3 is not offset by the suppression in κ_t . In most of the parameter space, the di-Higgs rate is enhanced through the suppression in λ_3 .

The horizontal lines in Fig. 6 show the projected sensitivity at the HL-LHC for the $bb\tau\tau$ channel (upper panel), and the $bb\gamma\gamma$ channel (lower panel) [67]. Most points lie below the

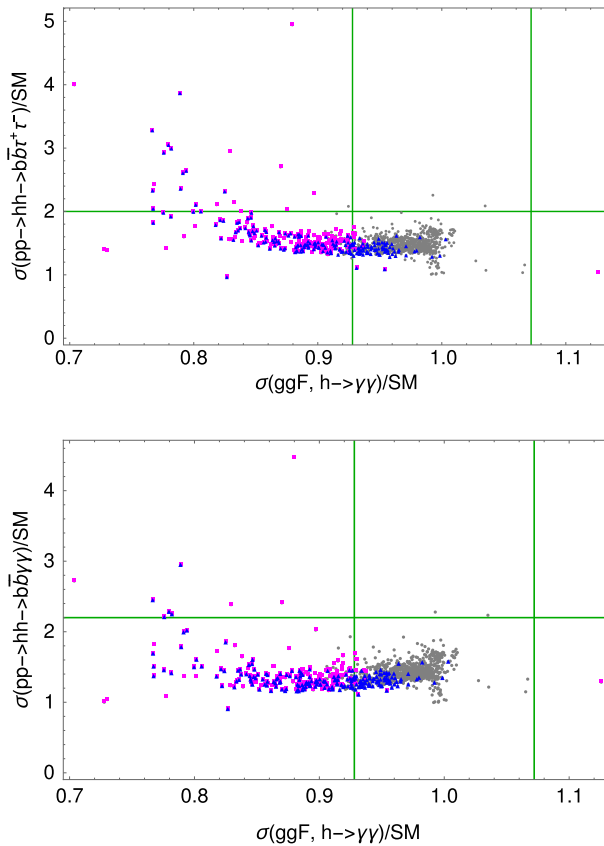


Fig. 6 Scatter plots for $\sigma(pp \rightarrow hh \rightarrow b\bar{b}\tau^+\tau^-)$ (upper panel) and $\sigma(pp \rightarrow hh \rightarrow b\bar{b}\gamma\gamma)$ (lower panel) normalized to SM value as a function of the SM-like Higgs boson production cross section via gluon-gluon fusion, with the SM-like Higgs boson decaying into $\gamma\gamma$ pair. All points satisfy current experimental constraints. The horizontal line is the 95% CL upper limit of the projected di-Higgs production cross section at HL-LHC [67]. The vertical lines are the 95% CL limits of the projected $\sigma(ggF, h \rightarrow \gamma\gamma)$ at HL-LHC. The magenta dots are outside the 95% CL of the projected SM-like Higgs boson production cross sections via other production modes and decay modes at HL-LHC. The blue dots are outside the 95% CL of the projected search for the additional neutral Higgs bosons in the di-tau final state at HL-LHC

horizontal lines, meaning the HL-LHC di-Higgs production measurements have very limited sensitivity in most regions of interest.

We also study the complementarity between di-Higgs and other Higgs measurements. In terms of precision Higgs measurements, we found that $h \rightarrow \gamma\gamma$ from gluon fusion is the most sensitive channel among all Higgs boson production modes and decay channels at the HL-LHC [71]. To compare with precision Higgs measurements, we plot the $h \rightarrow \gamma\gamma$ cross section from gluon fusion and overlay the projected sensitivity in this channel as the vertical lines at the HL-LHC. The $h \rightarrow \gamma\gamma$ measurement can probe a large fraction of the parameter space, and almost all points that can be tested by the di-Higgs measurement, can be tested by the $h \rightarrow \gamma\gamma$ measurement. To consider the sensitivity in precision Higgs measurements, we use magenta dots to represent points that can be tested by other Higgs coupling measurements.

Most points that can be tested by the $h \rightarrow \gamma\gamma$ measurement can be probed by other Higgs measurements as well, such as $h \rightarrow ZZ$ and $h \rightarrow WW$ measurements.

For direct searches of the heavy Higgs, we found that the search for heavy neutral Higgs bosons in the di-tau final state at HL-LHC [72] is a good complementary probe. We use blue dots to represent the points that can be tested in the heavy Higgs to di-tau channel. From Fig. 6, we can see that many blue dots lie between the two vertical lines, and below the horizontal line, showing direct searches of a heavy Higgs provides a complementary probe to precision Higgs and di-Higgs measurements. Combining di-Higgs, precision Higgs, and direct searches of the heavy Higgs, a large set of parameter points can be tested at the HL-LHC.

4 Conclusions

In this work, we have calculated the di-Higgs production cross section in the MSSM and the NMSSM at the one-loop level. We include the possible resonant contribution from new CP-even neutral Higgs states, new colored particles, and possible modifications in the Higgs couplings. We found that in both cases, the di-Higgs production can be enhanced significantly through a new resonance. As the new CP-even neutral Higgs bosons become heavy, di-Higgs production only enhances moderately due to the suppression in the Higgs self-couplings. The di-Higgs rate in the $bb\tau^+\tau^-$ final state can be further enhanced through the enhanced branching ratios. Given the current stop limit, we found the contributions from stops and other sfermions are small. Also, the interference effect is found to be small.

We further study the complementarity of di-Higgs measurement to other Higgs studies, including the precision measurement of the Higgs couplings and the search for new Higgs bosons. We found that there is a strong correlation in di-Higgs production rate and single Higgs production rate, especially outside the region where resonant di-Higgs dominates. Due to the complexity of the signature, and the small production cross section, di-Higgs measurements are not as sensitive as single Higgs measurements. The direct searches to new Higgs bosons, on the other hand, provide a complementary probe.

Acknowledgements We thank I. Lewis, K. Hagowara, and S. Heinemeyer for helpful discussions. This work is supported by University of Nebraska-Lincoln, National Science Foundation under Grant No. PHY-1820891, and the NSF Nebraska EPSCoR under Grant No. OIA-1557417.

A Form Factors

For the partonic process $g(p_1)g(p_2) \rightarrow h(k_1)h(k_2)$,

$$\begin{aligned}
 F_{\triangleright}^{(1/2)}(m_f) &= \frac{2m_f^2}{\hat{s}} [2 + (4m_f^2 - \hat{s})C_0(0, 0, \hat{s}, m_f^2, m_f^2, m_f^2)], \\
 F_{\square}^{(1/2)}(m_f) &= \frac{2m_f^2}{\hat{s}} \{m_f^2(8m_f^2 - \hat{s} - 2m_h^2)[D_0(0, 0, m_h^2, m_h^2, \hat{s}, \hat{u}, m_f^2, m_f^2, m_f^2, m_f^2) \\
 &\quad + D_0(0, 0, m_h^2, m_h^2, \hat{s}, \hat{t}, m_f^2, m_f^2, m_f^2, m_f^2) \\
 &\quad + D_0(0, m_h^2, 0, m_f^2, \hat{t}, \hat{u}, m_f^2, m_f^2, m_f^2, m_f^2)] \\
 &\quad + \frac{\hat{u}\hat{t} - m_h^4}{\hat{s}}(4m_f^2 - m_h^2)D_0(0, m_h^2, 0, m_h^2, \hat{t}, \hat{u}, m_f^2, m_f^2, m_f^2, m_f^2) + 2
 \end{aligned}
 \tag{A.1}$$

$$\begin{aligned}
 &+ 4m_f^2 C_0(0, 0, \hat{s}, m_f^2, m_f^2, m_f^2) + \frac{2}{\hat{s}}(m_h^2 - 4m_f^2) \\
 &[(\hat{t} - m_h^2)C_0(0, m_h^2, \hat{t}, m_f^2, m_f^2, m_f^2) + (\hat{u} - m_h^2)C_0(0, m_h^2, \hat{u}, m_f^2, m_f^2, m_f^2)] \}, \quad (A.2)
 \end{aligned}$$

$$\begin{aligned}
 G_{\square}^{(1/2)}(m_f) = &\frac{m_f^2}{\hat{s}} \left\{ 2(8m_f^2 + \hat{s} - 2m_h^2) \{ m_f^2 [D_0(0, 0, m_h^2, m_h^2, \hat{s}, \hat{u}, m_f^2, m_f^2, m_f^2, m_f^2) \right. \\
 &+ D_0(0, 0, m_h^2, m_h^2, \hat{s}, \hat{t}, m_f^2, m_f^2, m_f^2, m_f^2) \\
 &+ D_0(0, m_h^2, 0, m_h^2, \hat{t}, \hat{u}, m_f^2, m_f^2, m_f^2, m_f^2)] \\
 &- C_0(m_h^2, m_h^2, \hat{s}, m_f^2, m_f^2, m_f^2) \} - 2\{ \hat{s}C_0(0, 0, \hat{s}, m_f^2, m_f^2, m_f^2) \\
 &+ (\hat{t} - m_h^2)C_0(0, m_h^2, \hat{t}, m_f^2, m_f^2, m_f^2) + (\hat{u} - m_h^2)C_0(0, m_h^2, \hat{u}, m_f^2, m_f^2, m_f^2) \} \\
 &+ \frac{1}{ut - mh^4} \left\{ \hat{s}\hat{u}(8\hat{u}m_f^2 - u^2 - m_h^4)D_0(0, 0, m_h^2, m_h^2, \hat{s}, \hat{u}, m_f^2, m_f^2, m_f^2, m_f^2) \right. \\
 &+ \hat{s}\hat{t}(8\hat{t}m_f^2 - \hat{t}^2 - m_h^4)D_0(0, 0, m_h^2, m_h^2, \hat{s}, \hat{t}, m_f^2, m_f^2, m_f^2, m_f^2) \\
 &+ (8m_f^2 + \hat{s} - 2m_h^2)\{ \hat{s}(\hat{s} - 2m_h^2)C_0(0, 0, \hat{s}, m_f^2, m_f^2, m_f^2) \\
 &+ \hat{s}(\hat{s} - 4m_h^2)C_0(m_h^2, m_h^2, \hat{s}, m_f^2, m_f^2, m_f^2) \\
 &+ 2\hat{t}(m_h^2 - \hat{t})C_0(0, m_h^2, \hat{t}, m_f^2, m_f^2, m_f^2) \\
 &\left. + 2\hat{u}(m_h^2 - \hat{u})C_0(0, m_h^2, \hat{u}, m_f^2, m_f^2, m_f^2) \} \right\} \}, \quad (A.3)
 \end{aligned}$$

$$F_{\triangleright}^{(0)}(m_s) = \frac{-2m_s^2}{\hat{s}}(1 + 2m_s^2 C_0(0, 0, \hat{s}, m_f^2, m_f^2, m_f^2)), \quad (A.4)$$

$$\begin{aligned}
 F_{\square}^{(0)}(m_s, m_{s'}) = &\frac{-4m_s^2 m_{s'}^2}{\hat{s}} \left\{ \frac{m_h^2 - \hat{t}}{2\hat{s}} [C_0(m_h^2, 0, \hat{t}, m_{s'}^2, m_s^2, m_s^2) \right. \\
 &+ C_0(m_h^2, 0, \hat{t}, m_s^2, m_{s'}^2, m_{s'}^2)] + \frac{m_h^2 - \hat{u}}{2\hat{s}} [C_0(m_h^2, 0, \hat{u}, m_{s'}^2, m_s^2, m_s^2) \\
 &+ C_0(m_h^2, 0, \hat{u}, m_s^2, m_{s'}^2, m_{s'}^2)] + \frac{1}{2} \left(m_{s'}^2 - m_s^2 + \frac{\hat{u}\hat{t} - m_h^4}{\hat{s}} \right) \\
 &\cdot D_0(m_h^2, 0, m_h^2, 0, \hat{t}, \hat{u}, m_{s'}^2, m_s^2, m_s^2, m_{s'}^2) + m_s^2 [D_0(m_h^2, 0, m_h^2, 0, \hat{t}, \hat{u}, m_{s'}^2, m_s^2, m_s^2, m_{s'}^2) \\
 &+ D_0(m_h^2, m_h^2, 0, 0, \hat{s}, \hat{t}, m_s^2, m_{s'}^2, m_s^2, m_s^2) + D_0(m_h^2, m_h^2, 0, 0, \hat{s}, \hat{u}, m_s^2, m_{s'}^2, m_s^2, m_s^2)] \}, \quad (A.5)
 \end{aligned}$$

$$\begin{aligned}
 G_{\square}^{(0)}(m_s, m_{s'}) = &\frac{-2m_s^2 m_{s'}^2}{\hat{s}(m_h^4 - \hat{u}\hat{t})} \left\{ \hat{s}(2m_s^2 - 2m_{s'}^2 + \hat{t} + \hat{u})C_0(0, 0, s, m_s^2, m_s^2, m_s^2) \right. \\
 &- 2\hat{t}(m_h^2 - \hat{t})C_0(m_h^2, 0, \hat{t}, m_{s'}^2, m_s^2, m_s^2) - 2\hat{u}(m_h^2 - \hat{u})C_0(m_h^2, 0, \hat{u}, m_{s'}^2, m_s^2, m_s^2) \\
 &- (m_h^2 - \hat{t})(m_s^2 - m_{s'}^2)[C_0(m_h^2, 0, \hat{t}, m_s^2, m_{s'}^2, m_{s'}^2) + C_0(m_h^2, 0, \hat{t}, m_{s'}^2, m_s^2, m_s^2)] \\
 &- (m_h^2 - \hat{u})(m_s^2 - m_{s'}^2)[C_0(m_h^2, 0, \hat{u}, m_s^2, m_{s'}^2, m_{s'}^2) + C_0(m_h^2, 0, \hat{u}, m_{s'}^2, m_s^2, m_s^2)] \\
 &+ (2m_h^4 - \hat{t}^2 - \hat{u}^2)C_0(m_h^2, m_h^2, \hat{s}, m_s^2, m_{s'}^2, m_s^2) + [-\hat{s}(m_s^2 - m_{s'}^2)^2 \\
 &+ (m_s^2 + m_{s'}^2)(m_h^4 - \hat{u}\hat{t})] [D_0(m_h^2, 0, m_h^2, 0, \hat{t}, \hat{u}, m_{s'}^2, m_s^2, m_s^2, m_{s'}^2) \\
 &+ D_0(m_h^2, m_h^2, 0, 0, \hat{s}, \hat{t}, m_s^2, m_{s'}^2, m_s^2, m_s^2) + D_0(m_h^2, m_h^2, 0, 0, \hat{s}, \hat{u}, m_s^2, m_{s'}^2, m_s^2, m_s^2)] \\
 &- [\hat{s}\hat{t}^2 + (m_s^2 - m_{s'}^2)(2\hat{s}\hat{t} + \hat{u}\hat{t} - m_h^4)] D_0(m_h^2, m_h^2, 0, 0, \hat{s}, \hat{t}, m_s^2, m_{s'}^2, m_s^2, m_s^2) \\
 &- [\hat{s}\hat{u}^2 + (m_s^2 - m_{s'}^2)(2\hat{s}\hat{u} + \hat{u}\hat{t} - m_h^4)] D_0(m_h^2, m_h^2, 0, 0, \hat{s}, \hat{u}, m_s^2, m_{s'}^2, m_s^2, m_s^2) \}, \quad (A.6)
 \end{aligned}$$

where

$$\hat{s} = (p_1 + p_2)^2, \quad (\text{A.7})$$

$$\hat{t} = (p_1 - k_1)^2, \quad (\text{A.8})$$

$$\hat{u} = (p_1 - k_2)^2, \quad (\text{A.9})$$

and C_0 and D_0 are scalar three-point and four-point functions of one-loop integrals, defined as

$$C_0(p_1^2, p_2^2, (p_1 + p_2)^2, m_1^2, m_2^2, m_3^2) = \frac{\mu^{4-D}}{i\pi^{D/2} r_\Gamma} \int \frac{d^D q}{[q^2 - m_1^2][(q + p_1)^2 - m_2^2][(q + p_1 + p_2)^2 - m_3^2]}, \quad (\text{A.10})$$

$$D_0(p_1^2, p_2^2, p_3^2, p_4^2, (p_1 + p_2)^2, (p_2 + p_3)^2, m_1^2, m_2^2, m_3^2, m_4^2) = \frac{\mu^{4-D}}{i\pi^{D/2} r_\Gamma} \int \frac{d^D q}{[q^2 - m_1^2][(q + p_1)^2 - m_2^2][(q + p_1 + p_2)^2 - m_3^2][(q + p_1 + p_2 + p_3)^2 - m_4^2]}, \quad (\text{A.11})$$

where

$$r_\Gamma = \frac{\Gamma^2(1 - \epsilon)\Gamma(1 + \epsilon)}{\Gamma(1 - 2\epsilon)}, \quad D = 4 - 2\epsilon. \quad (\text{A.12})$$

The integrals are independent of μ in the limit $\epsilon \rightarrow 0$. We follow the conventions for momenta as stated in the manual of **LoopTools-2.15** [79].

References

1. G. Aad et al., Phys. Lett. B **716**, 1 (2012). <https://doi.org/10.1016/j.physletb.2012.08.020>
2. S. Chatrchyan et al., Phys. Lett. B **716**, 30 (2012). <https://doi.org/10.1016/j.physletb.2012.08.021>
3. V. Khachatryan et al., Phys. Rev. D **92**(1), 012004 (2015). <https://doi.org/10.1103/PhysRevD.92.012004>
4. G. Aad et al., Eur. Phys. J. C **75**(10), 476 (2015). <https://doi.org/10.1140/epjc/s10052-015-3685-1>, <https://doi.org/10.1140/epjc/s10052-016-3934-y>. [Erratum: Eur. Phys. J. C **76**, no.3,152(2016)]
5. Combined Higgs boson production and decay measurements with up to 137 fb⁻¹ of proton-proton collision data at $\sqrt{s} = 13$ TeV. Tech. Rep. CMS-PAS-HIG-19-005, CERN, Geneva (2020). <https://cds.cern.ch/record/2706103>
6. G. Aad et al., Phys. Rev. D **101**(1), 012002 (2020). <https://doi.org/10.1103/PhysRevD.101.012002>
7. C.Y. Chen, S. Dawson, I.M. Lewis, Phys. Rev. D **91**(3), 035015 (2015). <https://doi.org/10.1103/PhysRevD.91.035015>
8. P. Huang, A. Joglekar, B. Li, C.E.M. Wagner, Phys. Rev. D **93**(5), 055049 (2016). <https://doi.org/10.1103/PhysRevD.93.055049>
9. I.M. Lewis, M. Sullivan, Phys. Rev. D **96**(3), 035037 (2017). <https://doi.org/10.1103/PhysRevD.96.035037>
10. J. Alison, et al., in *Double Higgs Production at Colliders Batavia, IL, USA, September 4, 2018-9, 2018-9, 2019*, ed. by B. Di Micco, M. Gouzevitch, J. Mazzitelli, C. Vernieri (2019). <https://lss.fnal.gov/archive/2019/conf/fermilab-conf-19-468-e-t.pdf>
11. J. Cao, Z. Heng, L. Shang, P. Wan, J.M. Yang, JHEP **04**, 134 (2013). [https://doi.org/10.1007/JHEP04\(2013\)134](https://doi.org/10.1007/JHEP04(2013)134)
12. C. Han, X. Ji, L. Wu, P. Wu, J.M. Yang, JHEP **04**, 003 (2014). [https://doi.org/10.1007/JHEP04\(2014\)003](https://doi.org/10.1007/JHEP04(2014)003)
13. J. Cao, D. Li, L. Shang, P. Wu, Y. Zhang, JHEP **12**, 026 (2014). [https://doi.org/10.1007/JHEP12\(2014\)026](https://doi.org/10.1007/JHEP12(2014)026)
14. K.S. Babu, S. Jana, JHEP **02**, 193 (2019). [https://doi.org/10.1007/JHEP02\(2019\)193](https://doi.org/10.1007/JHEP02(2019)193)
15. B. Batell, M. McCullough, D. Stolarski, C.B. Verhaaren, JHEP **09**, 216 (2015). [https://doi.org/10.1007/JHEP09\(2015\)216](https://doi.org/10.1007/JHEP09(2015)216)

16. S. Dawson, A. Ismail, I. Low, Phys. Rev. D **91**(11), 115008 (2015). <https://doi.org/10.1103/PhysRevD.91.115008>
17. P. Huang, A. Joglekar, M. Li, C.E.M. Wagner, Phys. Rev. D **97**(7), 075001 (2018). <https://doi.org/10.1103/PhysRevD.97.075001>
18. C.Y. Chen, J. Kozaczuk, I.M. Lewis, JHEP **08**, 096 (2017). [https://doi.org/10.1007/JHEP08\(2017\)096](https://doi.org/10.1007/JHEP08(2017)096)
19. P. Basler, S. Dawson, C. Englert, M. Mühlleitner (2019)
20. M. Carena, Z. Liu, M. Riembau, Phys. Rev. D **97**(9), 095032 (2018). <https://doi.org/10.1103/PhysRevD.97.095032>
21. A.A. Barrientos Bendezu, B.A. Kniehl, Phys. Rev. **D64**, 035006 (2001). <https://doi.org/10.1103/PhysRevD.64.035006>
22. S. Dawson, C. Kao, Y. Wang, Phys. Rev. D **77**, 113005 (2008). <https://doi.org/10.1103/PhysRevD.77.113005>
23. E.W.N. Glover, J.J. van der Bij, Nucl. Phys. B **309**, 282 (1988). [https://doi.org/10.1016/0550-3213\(88\)90083-1](https://doi.org/10.1016/0550-3213(88)90083-1)
24. T. Plehn, M. Spira, P.M. Zerwas, Nucl. Phys. B **479**, 46 (1996). [https://doi.org/10.1016/0550-3213\(96\)00418-X](https://doi.org/10.1016/0550-3213(96)00418-X), [https://doi.org/10.1016/S0550-3213\(98\)00406-4](https://doi.org/10.1016/S0550-3213(98)00406-4). [Erratum: Nucl. Phys. B531,655(1998)]
25. A. Belyaev, M. Drees, O.J.P. Eboli, J.K. Mizukoshi, S.F. Novaes, Phys. Rev. D **60**, 075008 (1999). <https://doi.org/10.1103/PhysRevD.60.075008>
26. M. Spira. <http://tiger.web.psi.ch/proglist.html>
27. S. Heinemeyer, W. Hollik, G. Weiglein, Comput. Phys. Commun. **124**, 76 (2000). [https://doi.org/10.1016/S0010-4655\(99\)00364-1](https://doi.org/10.1016/S0010-4655(99)00364-1)
28. S. Heinemeyer, W. Hollik, G. Weiglein, Eur. Phys. J. C **9**, 343 (1999). <https://doi.org/10.1007/s100529900006>
29. G. Degrassi, S. Heinemeyer, W. Hollik, P. Slavich, G. Weiglein, Eur. Phys. J. C **28**, 133 (2003). <https://doi.org/10.1140/epjc/s2003-01152-2>
30. M. Frank, T. Hahn, S. Heinemeyer, W. Hollik, H. Rzehak, G. Weiglein, JHEP **02**, 047 (2007). <https://doi.org/10.1088/1126-6708/2007/02/047>
31. T. Hahn, S. Heinemeyer, W. Hollik, H. Rzehak, G. Weiglein, Phys. Rev. Lett. **112**(14), 141801 (2014). <https://doi.org/10.1103/PhysRevLett.112.141801>
32. H. Bahl, W. Hollik, Eur. Phys. J. C **76**(9), 499 (2016). <https://doi.org/10.1140/epjc/s10052-016-4354-8>
33. H. Bahl, S. Heinemeyer, W. Hollik, G. Weiglein, Eur. Phys. J. C **78**(1), 57 (2018). <https://doi.org/10.1140/epjc/s10052-018-5544-3>
34. U. Ellwanger, J.F. Guionie, C. Hugonie, JHEP **02**, 066 (2005). <https://doi.org/10.1088/1126-6708/2005/02/066>
35. U. Ellwanger, C. Hugonie, Comput. Phys. Commun. **175**, 290 (2006). <https://doi.org/10.1016/j.cpc.2006.04.004>
36. G. Degrassi, P. Slavich, Nucl. Phys. B **825**, 119 (2010). <https://doi.org/10.1016/j.nuclphysb.2009.09.018>
37. A. Djouadi, J. Kalinowski, M. Spira, Comput. Phys. Commun. **108**, 56 (1998). [https://doi.org/10.1016/S0010-4655\(97\)00123-9](https://doi.org/10.1016/S0010-4655(97)00123-9)
38. F. Domingo, U. Ellwanger, JHEP **12**, 090 (2007). <https://doi.org/10.1088/1126-6708/2007/12/090>
39. G. Belanger, F. Boudjema, C. Hugonie, A. Pukhov, A. Semenov, JCAP **0509**, 001 (2005). <https://doi.org/10.1088/1475-7516/2005/09/001>
40. S.P. Martin, Super Symmetry Primer **21**, 1–153 (2010). https://doi.org/10.1142/9789812839657_0001
41. H. Baer, X. Tata, *Weak Scale Supersymmetry: From Superfields to Scattering Events* (Cambridge University Press, Cambridge, 2006)
42. J.M. Campbell, J.W. Huston, W.J. Stirling, Rept. Prog. Phys. **70**, 89 (2007). <https://doi.org/10.1088/0034-4885/70/1/R02>
43. A.D. Martin, W.J. Stirling, R.S. Thorne, G. Watt, Eur. Phys. J. C **63**, 189 (2009). <https://doi.org/10.1140/epjc/s10052-009-1072-5>
44. D.B. Clark, E. Godat, F.I. Olness, Comput. Phys. Commun. **216**, 126 (2017). <https://doi.org/10.1016/j.cpc.2017.03.004>
45. S. Dawson, S. Dittmaier, M. Spira, Phys. Rev. D **58**, 115012 (1998). <https://doi.org/10.1103/PhysRevD.58.115012>
46. S. Borowka, N. Greiner, G. Heinrich, S.P. Jones, M. Kerner, J. Schlenk, U. Schubert, T. Zirke, Phys. Rev. Lett. **117**(1), 012001 (2016). <https://doi.org/10.1103/PhysRevLett.117.079901>, <https://doi.org/10.1103/PhysRevLett.117.012001>. [Erratum: Phys. Rev. Lett.117, no.7,079901(2016)]
47. S. Borowka, N. Greiner, G. Heinrich, S.P. Jones, M. Kerner, J. Schlenk, T. Zirke, JHEP **10**, 107 (2016). [https://doi.org/10.1007/JHEP10\(2016\)107](https://doi.org/10.1007/JHEP10(2016)107)

48. J. Baglio, F. Campanario, S. Glaus, M. Mühlleitner, M. Spira, J. Streicher, Eur. Phys. J. C **79**(6), 459 (2019). <https://doi.org/10.1140/epjc/s10052-019-6973-3>
49. A. Agostini, G. Degrassi, R. Gröber, P. Slavich, JHEP **04**, 106 (2016). [https://doi.org/10.1007/JHEP04\(2016\)106](https://doi.org/10.1007/JHEP04(2016)106)
50. K.L. Chan, U. Chattopadhyay, P. Nath, Phys. Rev. D **58**, 096004 (1998). <https://doi.org/10.1103/PhysRevD.58.096004>
51. H. Baer, V. Barger, P. Huang, JHEP **11**, 031 (2011). [https://doi.org/10.1007/JHEP11\(2011\)031](https://doi.org/10.1007/JHEP11(2011)031)
52. K.J. Bae, H. Baer, V. Barger, D. Sengupta, Phys. Rev. D **99**(11), 115027 (2019). <https://doi.org/10.1103/PhysRevD.99.115027>
53. U. Ellwanger, C. Hugonie, A.M. Teixeira, Phys. Rept. **496**, 1 (2010). <https://doi.org/10.1016/j.physrep.2010.07.001>
54. Search for direct top squark pair production in the 3-body decay mode with a final state containing one lepton, jets, and missing transverse momentum in $\sqrt{s} = 13\text{TeV}$ pp collision data with the ATLAS detector. Tech. Rep. ATLAS-CONF-2019-017, CERN, Geneva (2019). <https://cds.cern.ch/record/2676594>
55. Search for direct top squark pair production in events with one lepton, jets and missing transverse energy at 13 TeV. Tech. Rep. CMS-PAS-SUS-19-009, CERN, Geneva (2019). <https://cds.cern.ch/record/2682157>
56. N. Blinov, D.E. Morrissey, JHEP **03**, 106 (2014). [https://doi.org/10.1007/JHEP03\(2014\)106](https://doi.org/10.1007/JHEP03(2014)106)
57. A.M. Sirunyan et al., Eur. Phys. J. C **79**(5), 421 (2019). <https://doi.org/10.1140/epjc/s10052-019-6909-y>
58. A.M. Sirunyan et al., JHEP **09**, 007 (2018). [https://doi.org/10.1007/JHEP09\(2018\)007](https://doi.org/10.1007/JHEP09(2018)007)
59. M. Aaboud et al., JHEP **01**, 055 (2018). [https://doi.org/10.1007/JHEP01\(2018\)055](https://doi.org/10.1007/JHEP01(2018)055)
60. A.M. Sirunyan, et al., JHEP **07**, 126 (2020). [https://doi.org/10.1007/JHEP07\(2020\)126](https://doi.org/10.1007/JHEP07(2020)126)
61. A.M. Sirunyan et al., JHEP **01**, 096 (2020). [https://doi.org/10.1007/JHEP01\(2020\)096](https://doi.org/10.1007/JHEP01(2020)096)
62. A.M. Sirunyan et al., JHEP **07**, 142 (2019). [https://doi.org/10.1007/JHEP07\(2019\)142](https://doi.org/10.1007/JHEP07(2019)142)
63. M. Aaboud et al., JHEP **11**, 085 (2018). [https://doi.org/10.1007/JHEP11\(2018\)085](https://doi.org/10.1007/JHEP11(2018)085)
64. M. Aaboud et al., JHEP **09**, 139 (2018). [https://doi.org/10.1007/JHEP09\(2018\)139](https://doi.org/10.1007/JHEP09(2018)139)
65. W. Altmannshofer, M. Carena, N.R. Shah, F. Yu, JHEP **01**, 160 (2013). [https://doi.org/10.1007/JHEP01\(2013\)160](https://doi.org/10.1007/JHEP01(2013)160)
66. H.E. Logan, U. Nierste, Nucl. Phys. B **586**, 39 (2000). [https://doi.org/10.1016/S0550-3213\(00\)00417-X](https://doi.org/10.1016/S0550-3213(00)00417-X)
67. Measurement prospects of the pair production and self-coupling of the Higgs boson with the ATLAS experiment at the HL-LHC. Tech. Rep. ATL-PHYS-PUB-2018-053, CERN, Geneva (2018). <https://cds.cern.ch/record/2652727>
68. F. Goertz, A. Papaefstathiou, L.L. Yang, J. Zurita, JHEP **06**, 016 (2013). [https://doi.org/10.1007/JHEP06\(2013\)016](https://doi.org/10.1007/JHEP06(2013)016)
69. A. Azatov, R. Contino, G. Panico, M. Son, Phys. Rev. D **92**(3), 035001 (2015). <https://doi.org/10.1103/PhysRevD.92.035001>
70. A. Adhikary, S. Banerjee, R.K. Barman, B. Bhattacharjee, S. Niyogi, JHEP **07**, 116 (2018). [https://doi.org/10.1007/JHEP07\(2018\)116](https://doi.org/10.1007/JHEP07(2018)116)
71. Projections for measurements of Higgs boson cross sections, branching ratios, coupling parameters and mass with the ATLAS detector at the HL-LHC. Tech. Rep. ATL-PHYS-PUB-2018-054, CERN, Geneva (2018). <https://cds.cern.ch/record/2652762>
72. Prospects for the search for additional Higgs bosons in the ditau final state with the ATLAS detector at HL-LHC. Tech. Rep. ATL-PHYS-PUB-2018-050, CERN, Geneva (2018). <http://cds.cern.ch/record/2652284>
73. P. Basler, S. Dawson, C. Englert, M. Mühlleitner, Phys. Rev. D **99**(5), 055048 (2019). <https://doi.org/10.1103/PhysRevD.99.055048>
74. M. Carena, H.E. Haber, I. Low, N.R. Shah, C.E.M. Wagner, Phys. Rev. D **93**(3), 035013 (2016). <https://doi.org/10.1103/PhysRevD.93.035013>
75. G. Belanger, F. Boudjema, A. Pukhov, A. Semenov, Comput. Phys. Commun. **174**, 577 (2006). <https://doi.org/10.1016/j.cpc.2005.12.005>
76. G. Belanger, F. Boudjema, A. Pukhov, A. Semenov, Comput. Phys. Commun. **176**, 367 (2007). <https://doi.org/10.1016/j.cpc.2006.11.008>
77. G. Belanger, F. Boudjema, A. Pukhov, A. Semenov, Comput. Phys. Commun. **185**, 960 (2014). <https://doi.org/10.1016/j.cpc.2013.10.016>
78. N. Aghanim et al., *Planck 2018 results* (VI, Cosmological parameters, 2018)
79. T. Hahn, M. Perez-Victoria, Comput. Phys. Commun. **118**, 153 (1999). [https://doi.org/10.1016/S0010-4655\(98\)00173-8](https://doi.org/10.1016/S0010-4655(98)00173-8)